Tunable plasmon-enhanced second-order optical nonlinearity in transition-metal dichalcogenide nanotriangles

- F. Karimi, S. Soleimanikahnoj, I. Knezevic, "Tunable plasmon-enhanced second-order optical nonlinearity in transition-metal-dichalcogenide nanotriangles," *Phys. Rev. B* (Letter) 103, L161401 (2021).

The development of nanomaterials with a large nonlinear susceptibility is essential for nonlinear nanophotonics. We show that transition-metal dichalcogenide (TMD) nanotriangles have a large effective second-order susceptibility $\chi^{(2)}$ at mid-infrared to near-infrared frequencies owing to their broken centrosymmetry. $\chi^{(2)}$ is calculated within the density-matrix formalism that accounts for dissipation and screening. $\chi^{(2)}$ peaks in the vicinity of both two-photon resonances (specified by the geometry) and plasmon resonances (tunable via the carrier density). Aligning the resonances yields the values of $\chi^{(2)}$ as high as 10^{-6} m/V. In this paper, we show that equilateral nanotriangles made of single-layer TMDs such as MoS_2, WS_2, and WSe_2, whose growth has already been demonstrated, have a strong and electrically tunable second-order nonlinear optical response at midinfrared (mid-IR) to near-infrared (near-IR) frequencies. We calculate the second-order nonlinear optical response of these systems within the density-matrix quantum-transport framework that accounts for dissipative processes and screening in detail (excitonic effects are not considered). We show that the second-order susceptibility peaks in the vicinity of both two-photon intersubband resonances (whose positions are fixed by the nanotriangle geometry) and plasmon resonances (dynamically tunable by the carrier density). By tuning the carrier density to bring the plasmon and two-photon resonances into alignment, second-order susceptibility $\chi^{(2)}$ can become as high as 10^{-6} m/V, orders of magnitude higher than

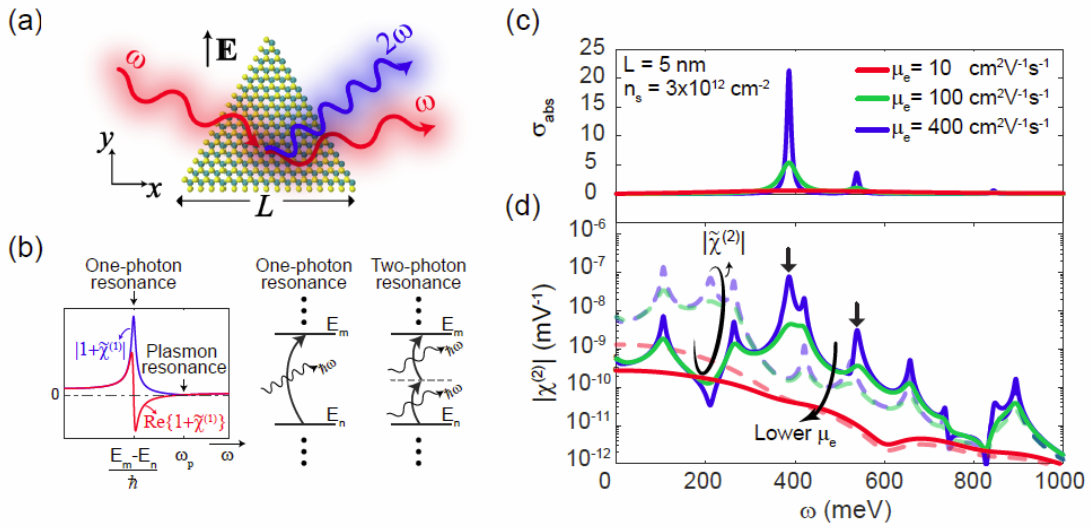

(a) Schematic of an equilateral TMD nanotriangle with the side length L. TM-polarized incident light causes linear as well as second-order nonlinear optical response. **(b)** One-photon, two-photon, and plasmon resonances. One- and two-photon resonances are due to intersubband optical transitions, whereas plasmon resonances are due to collective oscillations of electrons. **(c)** The loss function and (d) second-order susceptibility in response to external field (solid) and total field (dashed) of a 5-nm TMD nanotriangle with sheet density ns = 3×10^{12} cm^{-2} for different values of the electron mobility. The peaks marked by arrows correspond to two different plasmon resonances.

the intrinsic SHG of single-layer TMDs (~10^{-9} m/V) or the second-order susceptibility of bulk LiNbO3 (~10^{-11} m/V) at near-IR frequencies. The second-order optical response increases as the triangle size decreases. These findings underscore the suitability of single-layer TMD nanotriangles as an element for nonlinear nanophotonics, particularly second-harmonic generation.

Density-Matrix Model for Photon-Driven Transport in Quantum Cascade Lasers

- S. Soleimanikahnoj, M. L. King, and I. Knezevic, "Density-Matrix Model for Photon-Driven Transport in Quantum Cascade Lasers," *Phys. Rev. Applied* 15, 034045 (2021).
- S. Soleimanikahnoj, O. Jonasson, F. Karimi, I. Knezevic, "Numerically efficient density-matrix technique for modeling electronic transport in midinfrared quantum cascade lasers," *J. Comput. Electron*. 20, 280–309 (2021).

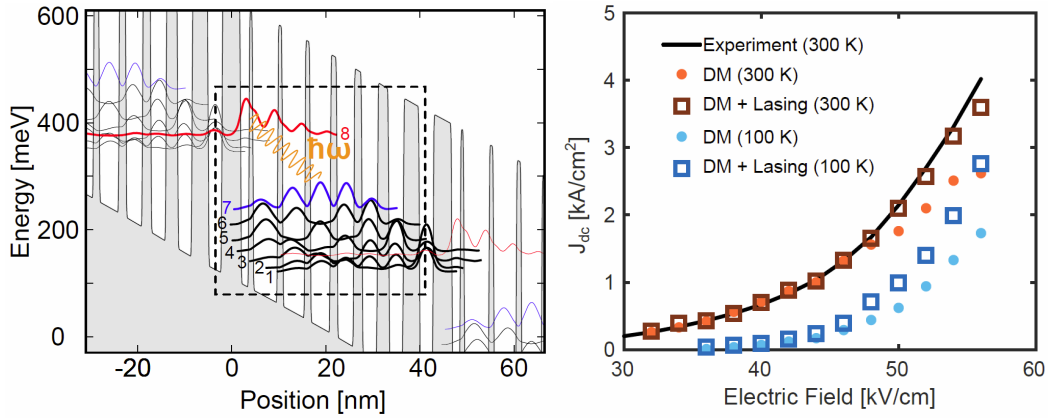

(Left) Conduction-band edge and probability densities for the eight eigenstates used in calculations (bold curves). The states that belong to neighboring periods are denoted by thin gray curves and the dashed box indicates a single stage, starting with the injection barrier. The bias electric field is 50 kV/cm. The states are numbered in the order of increasing energy, starting with the ground state. The radiative transition occurs from state 8 to state 7. **(Right)** Calculated *dc* current density as a function of the applied bias electric field at 100 K (blue) and 300 K (red), with (open squares) and without (solid circles) the influence of photon-assisted tunneling. Experimental data is given by the solid black curve.

Quantum cascade lasers (QCLs) are unipolar sources of coherent radiation emitting in the terahertz and infrared portions of the electromagnetic. The gain medium of a QCL is a periodic stack of compound-semiconductor heterostructures. The resulting multi-quantum-well electron band structure in the growth direction has discrete energy levels, and the associated wave functions are quasibound. While lasing stems from radiative electron transitions between specific states, nonradiative transitions mediated by various scattering mechanisms also play important roles in device operation. In particular, photon-assisted (PA) transport in terahertz and midinfrared QCLs is significant at and above lasing threshold, and appears particularly prominent in devices with diagonal design. There is a need for a computationally efficient

quantum-transport treatment of PA tunneling in QCLs that does not require phenomenological parameters and that employs broadly adopted intuitive concepts.

In this work, we present a quantum-mechanical model for photon-driven transport in QCLs that is computationally inexpensive, requires no phenomenological parameters, and is conducive to intuition building. The model stems from a rigorous theoretical framework with a positivity-preserving Markovian master equation of motion for the density matrix. The model is employed to characterize the steady-state and frequency response of a previously grown midinfrared QCL. Our results show that the inclusion of PA tunneling leads to substantial changes in electron transport around and above lasing threshold. Specifically, a significant increase in the current density is observed upon inclusion of PA tunneling, which allows for a significantly better agreement with experimental findings than the models that neglect this phenomenon. In particular, we show that, in quantum cascade lasers with diagonal design, photon resonances have a pronounced effect on electron dynamics around and above lasing threshold. This effect stems from a large spatial separation of the upper and lower lasing states.

Simulation Tool for Diffusion of Excitons in Carbon Nanotube Films

- S. W. Belling, Y. C. Li, A. H. Davoody, A. J. Gabourie, I. Knezevic, "DECaNT: Simulation Tool for Diffusion of Excitons in Carbon Nanotube Films," *J. Appl. Phys.* 129, 084301 (2021).

- Code available at https://github.com/li779/DECaNT

We developed the numerical tool DECaNT (https://github.com/li779/DECaNT) that simulates the diffusion of excitons in carbon nanotube thin films. We included resonance energy transfer processes that come from a microscopic theory and capture the effects of orientation, chirality, intertube distance, and environmental effects on exciton transfer rates. The tool uses Bullet Physics, a C++ library for simulating collisions, to create a 3D CNT mesh, which is then fed into our exciton ensemble Monte Carlo tool that tracks exciton position as these quasiparticles diffuse through the film. Based on the position--position correlation function, we calculated the diffusion tensor components and diffusion lengths. This tool is the first of its kind and allows for a new perspective on the behaviour of excitons in CNT films because it can help isolate the effects of parameters that are hard to individually control in experiment. In particular, we studied the impact of film morphology (alignment and bundling), chirality, intertube spacing, and defect density on cross-plane diffusion.

We found that films of aligned CNTs generally have higher cross-plane diffusion than films of random CNTs, because transfer rates are higher between aligned than between misoriented tubes. However, the impact of morphology is strongly dependent on the CNT size. The smallest CNTs, (4,2), have cross-plane diffusion properties that strongly depended on film morphology, while for all other chiralities in the simulation [(6,1),(6,5), and (8,7)], morphology has a much smaller effect. As CNT size increases, the center-to-center distance between scattering sites in different

CNTs also increases, and this increase in distance between scattering sites on different tubes overshadows the effect of relative orientation on the transfer rates between CNTs.

We found that adding intertube spacing always reduces cross-plane diffusion, but the rate at which diffusion decreases with distance depends on morphology. The fastest decrease is observed in aligned films, followed by randomly oriented and bundled films.

To analyze the effect of defect density (``quenching sites'') on the transport properties of CNT films, we calculated the exciton lifetime and diffusion length. We found that in-plane diffusion is isotropic and the associated length is about three times larger than the cross-plane diffusion length. As expected, the diffusion length decreases with increasing quenching-site density.

In short, DECaNT is a new open-source tool that offers the ability to isolate and study a number of film properties such as morphology, intertube spacing, chirality, and defect density on exciton transport in CNT films.

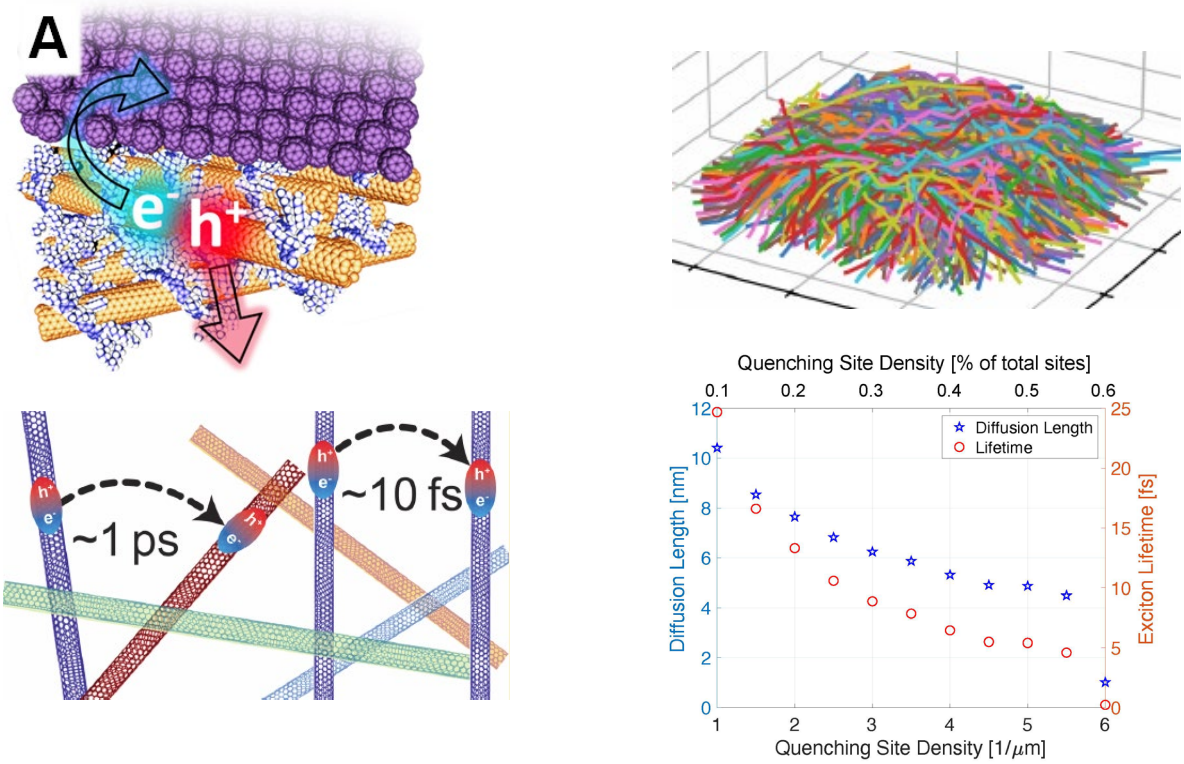

(Top left) Schematic of exciton dissociation a thte interface between a carbon nanotube film and a C60 layer. **(Top right)** Numerically generated carbon nanotubes film. **(Bottom left)** Shecmatic of exciton transfer between nanotubes and characteristic rates (fast between similar parallel tubes, slow between different misoriented tubes. **(Bottom right)** Calculation of diffusion length in DECaNT.

Dielectric waveguides with embedded graphene nanoribbons for all-optical broadband modulation

- F. Karimi and I. Knezevic, *Opt. Mater. Express* 9(11), 4456-4463 (2019).

All-optical processing offers low power consumption and fast operation speed and is a promising approach to high-bit-rate communication. Realization of all-optical integrated photonics requires core materials that strongly mediate photon–photon interaction. Recently, it was shown that, in the long-wavelength limit, graphene nanoribbons (GNRs) have a very strong Kerr optical nonlinearity at the telecom wavelength range (1.3-1.6 μm). In this paper, we design, numerically model, and simulate a dielectric waveguide with embedded GNRs for all-optical SAM applications. Owing to the strongly field-dependent susceptibility of GNRs, the proposed design has a broad BW and a very compact footprint. First, we characterize the GNR optical nonlinearity via the density matrix theoretical formalism that carefully accounts for material-specific properties and scattering mechanisms. Then, we design a vdW heterostructure comprising undoped GNRs and hexagonal boron nitride (hBN) sheets. We embed the GNR-hBN vdW heterostructure (GBNH) in a rib silicon waveguide and optimize it for the maximum optical concentration near the GBNH. The GBNH employed here are well within current experimental capabilities. Encasing in hBN enables the stacking of GNRs with high density without changing the individual GNR's electronic or optical properties. hBN also protects undoped GNRs from unintentional doping. We show that implanting different-width GNRs in the GBNH broadens the saturable absorption BW. Also, by increasing the number of GNR layers in the GBNH, the modulation strength rises up to 0.03 dB/μm over the telecom frequency range, which removes the need for dynamical tuning. For narrowband applications, an appropriately engineered GBNH yields even larger modulation depth, as large as 0.7 dB/ dB/μm. The combined advantages of small footprint, low power consumption, large modulation depth, and broad BW underscore the capability of the GBNH-based dielectric waveguide as a saturable absorber for ultrafast pulse generation applications [9].

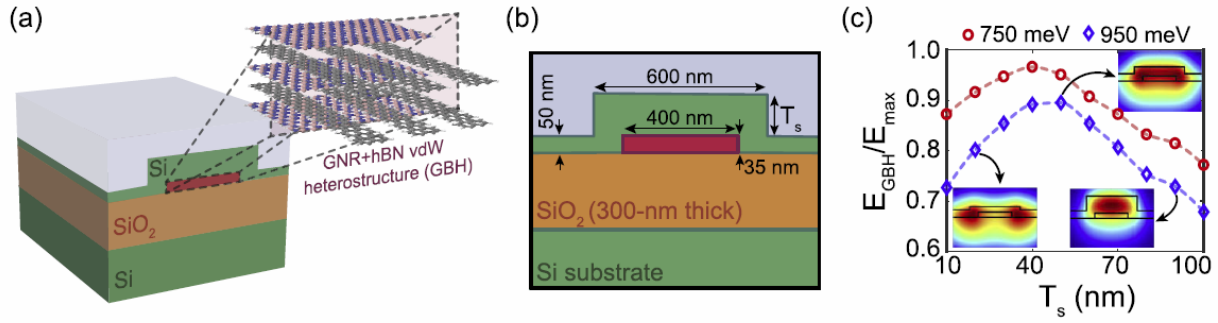

(a) Schematic of a GBNH-embedded rib silicon waveguide. The zoomed-in heterostructure consists of graphene nanoribbons (gray) encased in hBN (pink). **(b)** The cross-section view of the waveguide. **(c)** E_{GBNH}/Emax as a function of the silicon strip thickness, Ts. EGBNH denotes the electric field at the center of the E_{GBNH} and Emax is the maximal electric field across the device. The closer the ratio is to unity, the more concentrated the optical field is near the GBNH. Ts ~ 45 nm yields optimal optical confinement. The insets show the electric-field profile across the waveguide for narrow (Ts = 20 nm), optimal (Ts = 45 nm), and thick (Ts = 100 nm) silicon strips at 950 meV.

Measurements of the thermal resistivity of InAlAs, InGaAs and InAlAs/InGaAs Superlattices

G. R. Jaffe, S. Mei, C. Boyle, J. D. Kirch, D. E. Savage, D. Botez, L. J. Mawst, I. Knezevic, M. G. Lagally, and M. A. Eriksson, *ACS Appl. Mater. Interfaces* 11, 11970-11975 (2019).

Thermal management efforts in nanoscale devices must consider both the thermal properties of the constituent materials and the interfaces connecting them. It is currently unclear whether alloy/alloy semiconductor superlattices such as InAlAs/InGaAs have lower thermal conductivities than their constituent alloys. We report measurements of the crossplane thermal resistivity of InAlAs/InGaAs superlattices at room temperature, showing that the superlattice resistivities are larger by a factor of 1.2–1.6 than that of the constituent bulk materials, depending on the strain state and composition. We show that the additional resistance present in these superlattices can be tuned by a factor of 2.5 by altering the lattice mismatch and thereby the phonon-mode mismatch at the interfaces, a principle that is commonly assumed for superlattices but has not been experimentally verified without adding new elements to the layers. We find that the additional resistance in superlattices does not increase significantly when the layer thickness is decreased from 4 to 2 nm. We also report measurements of 250–1000 nm thick films of undoped InGaAs and InAlAs lattice-matched to InP substrates, for there is no published thermal conductivity value for the latter, and we find it to be 2.24 ± 0.09 at 22 °C, which is ~2.7 times smaller than the widely used estimates.

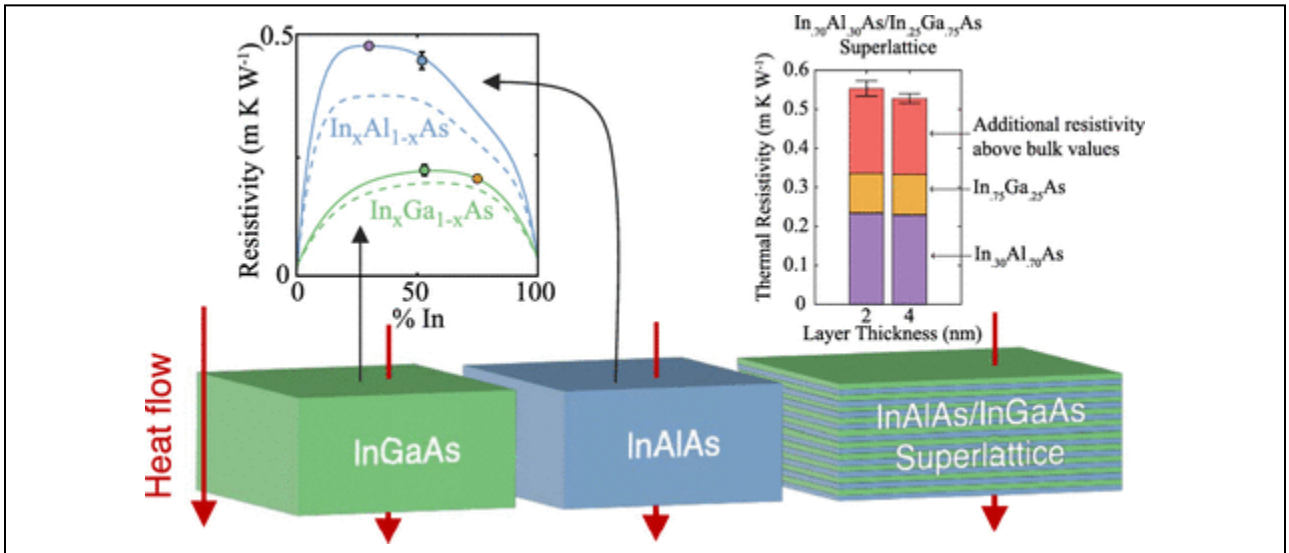

(Main panel) Experiment schematic. **(Top left inset)** Measured thermal resistivity of InAlAs (blue point) and InGaAs (green point) as a function of alloy concentration. The inset also includes a calculation of the thermal resistivity of both alloys using the virtual crystal approximation. The mass–difference scattering rate of the original calculation in (dashed lines) was scaled (solid lines) to match the measured resistivities, thereby providing an estimate for the resistivity of the alloys in the strain balanced superlattices (orange and purple points), which could not be measured. (**Top right inset)** The total bar height is the measured resistivity of a) lattice matched and b) strain balanced superlattices with colored bars indicating what the resistivity of an equivalent amount of the constituent alloys with no interfaces would be. All the superlattices are more resistive than equivalent amounts of their bulk constituents, and the red bars indicate that increase in resistivity. The resistivity of the alloys in the lattice matched superlattices were directly measured, and the resistivities of the alloy compositions in the strain balanced superlattices are extracted from the virtual crystal approximation calculation shown in the top left inset.